ADVANCED OPTICAL MATERIALS
www.advopticalmat.de

Fourier Control of Air Modes in High-Q Metasurfaces

Guilherme S. Arruda, Vinicius M. Pepino, Ben-Hur V. Borges, and Emiliano R. Martins*

Dielectric metasurfaces supporting high-quality factor (high-Q) resonances, e.g., through bound states in the continuum, have attracted significant interest from the scientific community. Air modes can significantly improve the performance and functionality of metasurfaces, for example, by enhancing mode sensitivity and reducing material absorption. Here, the concept of air-guided mode resonances with Fourier control of the resonance Q-factor with a double-ridge metasurface supporting air modes is introduced and experimentally demonstrated. It is shown that the Q-factor can be easily Fourier controlled all the way to infinity by adjusting the gap width, and that the energy confinement in air is largely independent of the gap width. As an application example, it is shown that the Q-factor of air modes is decoupled from material losses, thus allowing a Q-factor enhancement of up to 12× when compared to conventional (single-ridge) metasurfaces. This design offers an easy way to control the Q-factor of air modes, thus opening the possibility of achieving high-Q in metasurfaces using lossy materials.

1. Introduction

High-quality factor (high-Q) photonic resonances play a central role in many key applications such as sensing,[1] lasing,[2] harmonic generation,[3] Raman scattering,[4] filtering,[5] and so on. In recent years, much attention has been turned toward resonances accessed from free space.[6–9] In particular, all dielectric metasurfaces[10] supporting bound states in the continuum (BICs) have been shown to support resonances with quality factors (Q-factors) of the order of hundreds of thousands.[11]

In principle, these resonances Q-factor can be as high as the designer wishes, theoretically extending all the way to infinity (for lossless systems). In practice, however, the Q-factor is limited by material and scattering losses. Thus, such high-Q resonances are typically obtained using high index materials with low extinction coefficients κ.[11–15] Losses also affect the resonance amplitude, even more dramatically than they affect the Q-factor.[16] These effects limit the designer's choice of materials and frequency of operation for high-Q resonances. Tunable metasurfaces, for example, often use absorbing materials in the visible regime, such as ITO,[17] Sb_2S_3,[18] and GaAs.[19] Low-cost materials compatible with mass production techniques, such as silicon, also share the same limitations.[20,21] Tackling losses, therefore, is a problem of paramount importance to extend the applicability of metasurfaces into practical devices. This problem has been largely approached using optimization methods,[22,23] and an interesting exception relies on hybridization between lossy and nonlossy resonances.[24] A promising and simple approach, however, is to use the so called "air" or "slot" modes, in which the electromagnetic energy is mostly confined in air.[25,26] Air modes are also intrinsically more sensitive to alterations on the nearby environment, which finds applications in sensors,[27–33] in tunable metasurfaces,[34] and underlie the extraordinary transmission effect,[35–37] which can be used to obtain high-Q resonances (up to ≈2400), e.g., through interference between asymmetric metal hole dimmers[38] or through asymmetric coupling between metal holes.[39] A systematic approach to combine the advantage of high-Q resonances with the higher sensitivity and lower modal losses of air modes is, however, still missing.

Here, we introduce the concept of air-guided mode resonances (AGMR) with Fourier control of the Q-factor. Guided mode resonances (GMR) constitute an important class of resonances with applications in lasers,[40] sensors,[6,7] and signal processing,[41,42] and can be easily adapted for any frequency of operation. Our design uses a unit cell consisting of two ridges, supporting an air mode whose Q-factor can be easily controlled, all the way to infinity (for lossless systems). In this design, the GMR energy is mostly confined in the air gap between the ridges, thus constituting an AGMR. As an example of application, we show that the presence of the air mode significantly reduces the losses, and that the Q-factor can be easily Fourier controlled by adjusting the gap width. We show that enhancements of about 12× can be achieved with amorphous silicon and up to 5.4× can be achieved with a 3D printing resin (Anycubic Craftsman Resin). We also 3D print a metasurface using this resin and experimentally demonstrate a Q-factor enhancement of 3.3× without sacrificing the resonance amplitude.

2. Fourier Control of AGMRs Q-Factors

We begin by investigating the conditions for the appearance of air modes in double-ridge metasurfaces, as illustrated in **Figure 1**a. The structure consists of an array of dielectric ridge pairs (relative permittivity $\epsilon_r = 2.66$, see the Experimental Section), with

G. S. Arruda, V. M. Pepino, B.-H. V. Borges, E. R. Martins
São Carlos School of Engineering
Department of Electric and Computer Engineering
University of São Paulo
São Carlos, SP 13566-590, Brazil
E-mail: guilherme.simoneti.arruda@usp.br

The ORCID identification number(s) for the author(s) of this article can be found under https://doi.org/10.1002/adom.202301563

DOI: 10.1002/adom.202301563

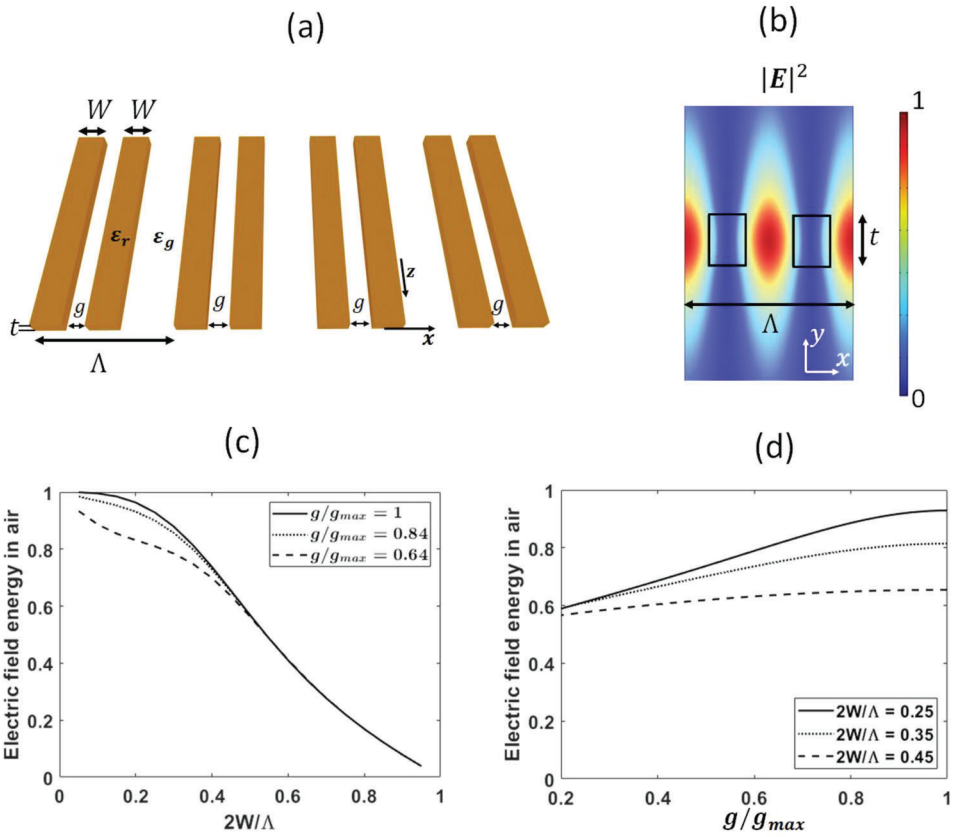

Figure 1. a) Schematic of the metasurface supporting an AGMR. b) Typical electric intensity distribution of a TE polarized air mode supported by the structure. Only the cross section of a single unit cell is displayed (the dielectric blocks are highlighted in the black rectangles). The geometric parameters are: $2W = 0.45\Lambda$, $g = g_{max} = 0.5\Lambda - W$, $t = 0.31\Lambda$, and frequency $\omega_0 = 2\pi c/1.02\Lambda$. The proportion between the electric field energy ($\epsilon|\boldsymbol{E}|^2$) inside the low index region and the entire periodic layer (of thickness $t = 0.31\Lambda$) is also shown as function of c) W and d) g. The modes were accessed at frequencies ranging from $2\pi c/1\Lambda$ (lowest W) to $2\pi c/1.28\Lambda$ (highest W). TE polarization was assumed.

thickness t, period Λ, width W, and gap width g. An air mode is characterized by a highly confined electric field energy in the air gap (or low index region),[25] as illustrated in Figure 1b. Note that such a structure supports modes propagating in the x-direction (Figure 1a), which is parallel to the direction of the periodicity.[43] The TE (electric field parallel to the z-axis) air mode confinement dependence on the ridge and gap widths are shown in Figure 1c,d, respectively.

The requirement of a double-ridge unit cell to support an air mode is apparent from Figure 1c: regardless of the gap width, the field concentration scales with the inverse of the ridge width. Moreover, according to Figure 1d, wide gaps (large g) contribute to a higher concentration of the electric field in air. Indeed, the highest electric field energy concentration in air occurs precisely when the gap distance is the highest possible, that is, $g = g_{max} = 0.5\Lambda - W$ (the parameter g_{max} is defined as the gap width for which the metasurface period is halved). Therefore, the conditions for the appearance of air modes are small W and large g. For more details on the field distribution and the mode's dispersion see Section S1 (Supporting Information).

The resonance Q-factor arising from the excitation of these air modes can be easily controlled by adjusting the structure's Fourier components.[44] To understand how such control comes about, first consider the excitation of a GMR[45] in a slab waveguide coupled by a shallow grating (the shallow grating is not a requirement, but it is assumed for the sake of simplicity). The diffraction components are described by Bragg's equation

$$k_{diff} = k_i + m\frac{2\pi}{\Lambda} \tag{1}$$

where k_i and k_{diff} are, respectively, the incident and diffracted wavevector components parallel to the grating (along the x-direction in **Figure 2**), and m is an integer number describing the grating order.

As represented in Figure 2a, the first-order component ($m = \pm 1$) mediates coupling of radiating and waveguided modes. A waveguide mode with effective index n_{eff} has wavevector components given by $\pm (2\pi/\lambda_0)n_{eff}$, where λ_0 is the free space wavelength. To excite a waveguide mode, the condition $k_{diff} = \pm (2\pi/\lambda_0)n_{eff}$ must be satisfied. Thus, according to Equation (1) and assuming perpendicular incidence ($k_i = 0$), a waveguide mode is excited when the period Λ is given by

$$\frac{2\pi}{\Lambda} = \frac{2\pi}{\lambda_0} n_{eff} \tag{2}$$

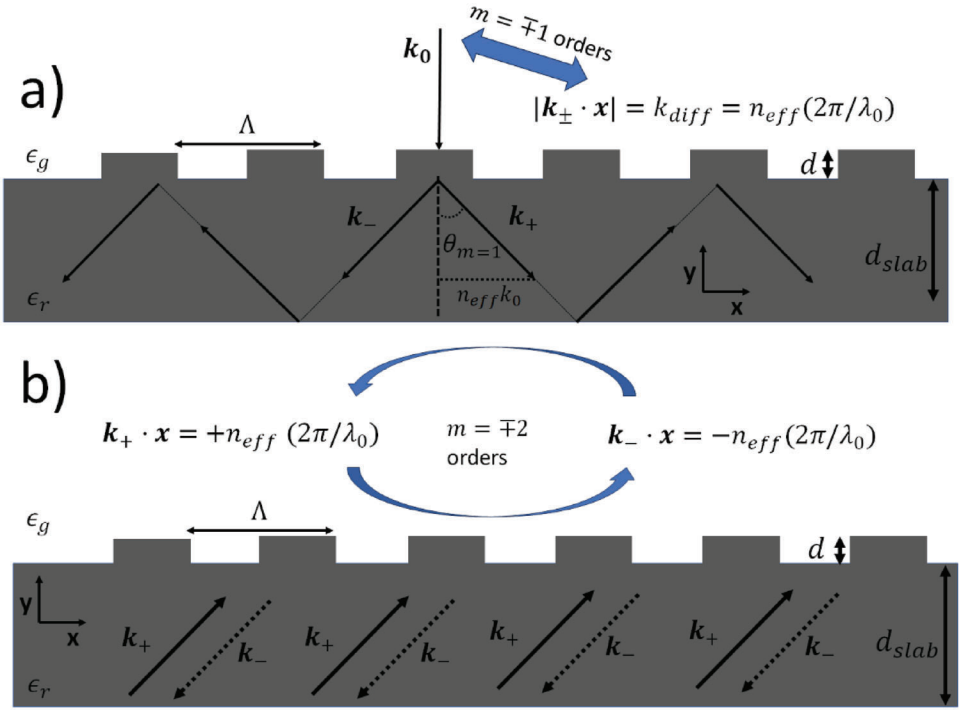

Figure 2. Schematics of slab dielectric waveguides with thickness d_{slab} with a shallow grating (period Λ and thickness $d < d_{slab}$) on their surface. A GMR of effective index n_{eff} is excited by a perpendicularly incident plane wave (wavevector $\boldsymbol{k}_0$), provided the period matches the condition of Equation (2). a) The coupling of radiating and guided modes is mediated by the first-order components [$m = \mp 1$, see Equation (2)]. b) The second-order components [$m = \mp 2$, see Equation (3)] mediate coupling of counter propagating modes. The waves leaking out of the structure (reflected and transmitted waves) were omitted in the schematics.

Besides coupling radiating and waveguided modes, the grating also couples counter-propagating waveguide modes. Such coupling is mediated by second-order diffraction. Indeed, according to Equation (1), a waveguide mode $k_i = \pm(2\pi/\lambda_0)n_{eff}$ is diffracted into a counterpropagating mode $k_{diff} = -k_i$ by the $m = \mp 2$ orders

$$k_{diff} = k_i + m\frac{2\pi}{\Lambda} = \pm\frac{2\pi}{\lambda_0}n_{eff} \mp 2\frac{2\pi}{\lambda_0}n_{eff} = \mp\frac{2\pi}{\lambda_0}n_{eff} = -k_i \quad (3)$$

Thus, according to Equation (3), second-order diffraction mediates coupling of counter-propagating modes. This process is illustrated in Figure 2b.

Since coupling is mediated by the first and second order diffraction components, the strengths of the coupling processes depend on the structure's corresponding Fourier components.[46,47] Expressing the dielectric constant as a Fourier series

$$\epsilon(x) = \sum_p \epsilon_p e^{-\frac{i2\pi p}{\Lambda}x} \quad (4)$$

where p is an integer, it follows that first-order coupling (between radiating and guided modes) depends on the first-order Fourier component ϵ_1, while the second-order coupling (between counter-propagating modes) depends on the second-order Fourier component ϵ_2. Explicit expressions for such dependences in the limit of shallow gratings were derived by Kazarinov et.al.,[48] and are given by

$$h_1 = |\epsilon_1|^2 \frac{\pi^2\Lambda(\varepsilon_r - \varepsilon_g)}{\lambda_0^3\sqrt{n^2 - n_{eff}^2}}\left|\int_0^d e^{i\frac{2\pi}{\lambda_0}\sqrt{n^2-n_{eff}^2}y}\phi(y)\,dy\right| \quad (5)$$

$$h_2 = -\epsilon_2\frac{\pi\Lambda(\varepsilon_r - \varepsilon_g)}{\lambda_0^2}\int_0^d \phi^2(y)\,dy \quad (6)$$

where n is the refractive index of the slab material ($n = \varepsilon_r^2$), h_1 and h_2 are, respectively, the first- and second-order coupling coefficients, $\phi(y)$ is the mode's field distribution and the integration runs over the grating thickness.

Since h_1 couples radiating and guided modes, and h_2 couples counter-propagating modes, it is possible to control the Q-factor by tuning ϵ_1 and ϵ_2. In particular, first order coupling vanishes if $\epsilon_1 = 0$; consequently, the Q-factor goes to infinity at this condition, since the mode becomes fully guided. In general, the Q-factor scales with the ratio of $|\epsilon_2|$ to $|\epsilon_1|$ (an example is shown later in Figure 4b).

Even though the discussion above assumed a slab waveguide coupled to a shallow grating, the same considerations also pertain to the coupling mechanisms of the double-ridge metasurface, with the caveat that the mode effective index is no longer of a conventional slab waveguide, but of a corrugated slab (such as the subwavelength grating waveguides[49]). A key feature of the

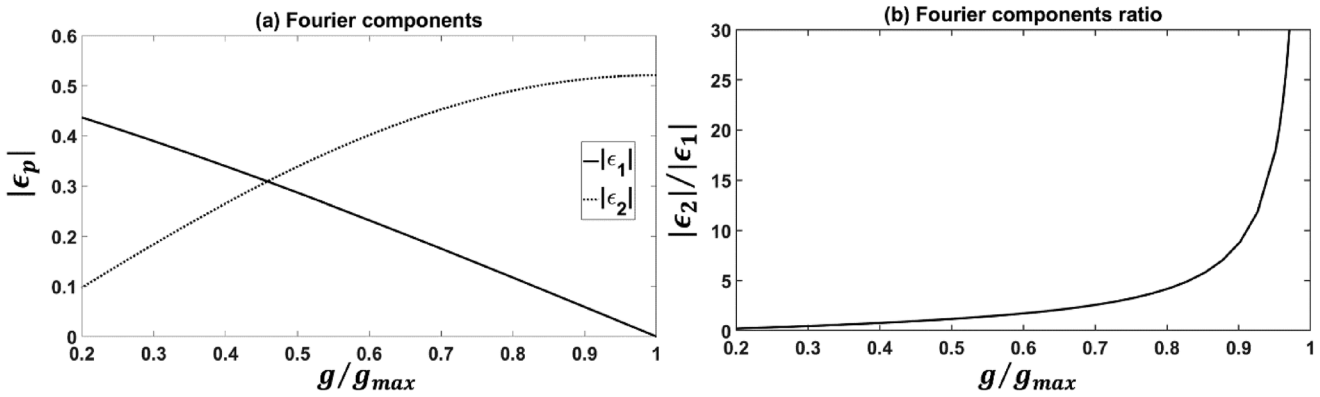

Figure 3. a) Magnitude of the first and second (ϵ_1 and ϵ_2, respectively) Fourier components of the grating and b) their ratio as a function of the gap distance g of the double-ridge structure considering $\Lambda = 9.75$ mm and $2W = 0.45\Lambda$.

double-ridge metasurface, however, is that it favors an especially convenient control over ϵ_2 and ϵ_1, whose ratio can be tuned all the way to infinity. Indeed, for the double-ridge metasurface, the ϵ_p components are given by (see Section S2, Supporting Information, for a derivation and Section S3, Supporting Information, for the relation between the FF and the Fourier components of the single-ridge metasurface)

$$\epsilon_p = 2\cos\left[-\frac{\pi}{\Lambda}p\left(g+W\right)\right]\frac{\sin\left(\frac{p\pi W}{\Lambda}\right)}{p\pi}\left(\epsilon_r-\epsilon_g\right);\ p\neq 0. \tag{7}$$

Using Equation (7), plots of $|\epsilon_1|$, $|\epsilon_2|$ (**Figure 3**a) and of the ratio $|\epsilon_2|/|\epsilon_1|$ (Figure 3b) as a function of g for fixed W are shown in Figure 3. Notice that, when $g = g_{max} = 0.5\Lambda - W$, this ratio goes to infinity, as ϵ_1 goes to zero (at the condition $g = g_{max}$, the period is effectively halved, and hence the second-order Fourier component of the original period becomes the first-order component of the half period). Thus, at this condition the mode becomes fully guided, and consequently the Q-factor goes to infinity.

An important advantage of such Q-factor Fourier control afforded by the double-ridge metasurface supporting air modes is its robustness to losses. To understand the physical origin of this advantage, we differentiate between the radiative Q_r, the nonradiative Q_{nr} and the total Q_t. Q_r is the design, or ideal Q-factor, that is, the Q-factor in the absence of any losses other than the radiative losses (which are the losses associated with the coupling with radiating modes). Q_{nr}, on the other hand, captures the effect of undesired losses, such as absorption or scattering, and it is infinite in the ideal case. Finally, Q_t is the total Q-factor, arising from the combination of Q_r and Q_{nr}, and given by[16]

$$Q_t^{-1} = Q_r^{-1} + Q_{nr}^{-1} \tag{8}$$

In a conventional singe ridge metasurface, on the one hand, Q_r scales with the fill factor ($FF = W/\Lambda$, see inset of **Figure 4**a), as shown in Figure 4a. The field confinement in the dielectric, however, also increases with the FF. Therefore, in a conventional structure, designs aiming to increase Q_r also result in an increase of energy concentration in the dielectric (due to the higher FF), and hence higher losses, entailing lower Q_{nr} and Q_t. In the double-ridge metasurface, on the other hand, Q_r, as controlled by the ratio $|\epsilon_2|/|\epsilon_1|$, does not come at the expense of higher losses, because the field remains confined in air. To illustrate the impact of Fourier control of air modes, we show the dependence of Q_r on the ratio $|\epsilon_2|/|\epsilon_1|$ for the AGMR (Figure 4b) and compare the effect of losses on the GMR and AGMR with the same Q_r. We select different values of Q_r, and show the corresponding GMR (black lines) and AGMR (red lines) resonances in Figure 4c assuming material absorption losses ($\epsilon_r = 2.66 - i0.08$, solid lines) and the lossless ideal case ($\epsilon_r = 2.66$, dashed lines). Notice that, in all cases, the same Q_r results in a higher Q_t for the AGMR as compared to the GMR, as evident by the thinner AGMR solid peak curves, and also resonances with higher peaks (which set the limits of detection of photonic resonances[16]), to the limit when the GMR completely disappears while it is still possible to detect the AGMR ($Q_r = 3200$). The higher AGMR Q_t and resonance amplitudes are due to the lower losses, which entails higher Q_{nr} for the AGMR as compared to the GMR.

The advantages of Fourier controlling the AGMR are quantified in **Figure 5**, which shows the Q_{nr} (dashed lines) and energy confinement in air (solid lines) as a function of Q_t for the AGMR supported by the double-ridge metasurfaces (red lines) and the GMR supported by single-ridge metasurfaces (black lines). We assume the geometries of Figure 4 and $\epsilon_r = 2.66 - i0.08$ (to obtain Q_r we set $\epsilon_r = 2.66$, for Q_t we set $\epsilon_r = 2.66 - i0.08$, and for Q_{nr} we use Equation (8); see Section S4 (Supporting Information) for more details on the dependence of Q_t on material losses). The Q-factors are changed by varying the gap width g in the double-ridge metasurface and the FF in the single-ridge metasurface. Solid lines correspond to the fraction of energy confined in air, whereas dashed lines correspond to the modal losses as expressed by Q_{nr}. On the one hand, the GMR Q_t (black lines) can only be increased by increasing the FF, which comes at the expense of higher energy confinement in the lossy dielectric (i.e., lower energy confinement in air – solid black lines), thus resulting in higher modal losses (lower Q_{nr} – dashed black lines). For these reasons, only modest values of Q_t are accessible by the GMRs. On the other hand, Fourier control of the air mode allows the AGMR's Q_t to increase without significant loss penalty (dashed red lines), since the mode remains confined in air (solid red line) for a wide range of Q_t. Therefore, the AGMR can access higher values of Q_t. In Figure 5, the theoretical maximum gain for Q_t is 6.5×, because the GMR is limited to $Q_t = 40$ while

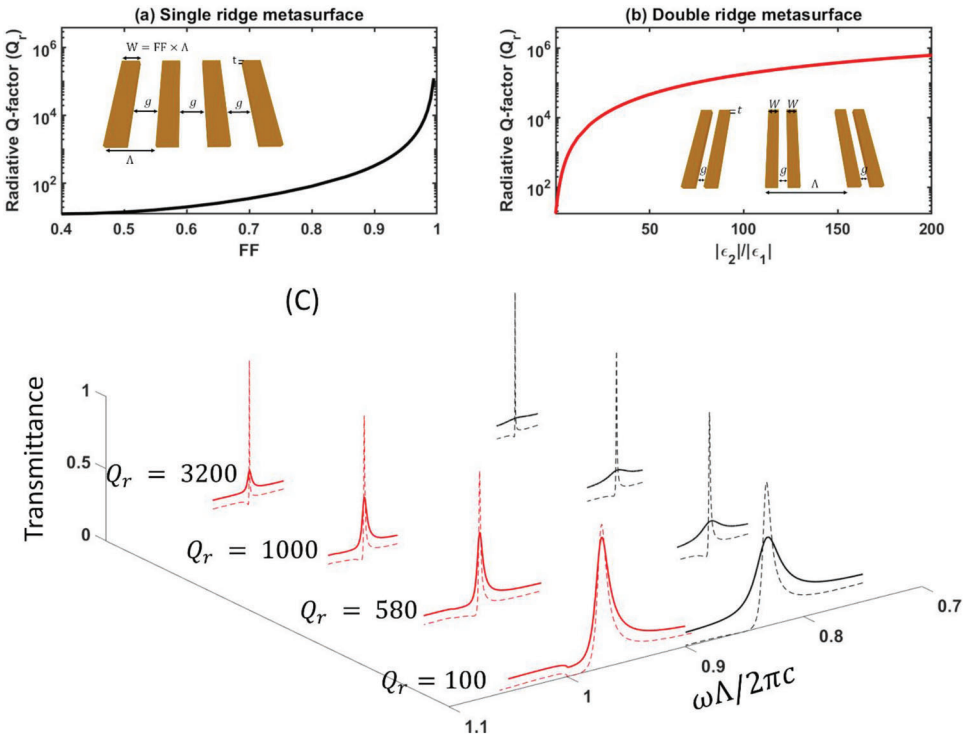

Figure 4. a) Dependence of Q_r on *FF* of a conventional single-ridge metasurface (inset), $t = 0.33\Lambda$ with ω_0 ranging from $2\pi c/1.09\Lambda$ (lowest FF) to $2\pi c/1.32\Lambda$ (highest FF). b) Dependence of Q_r on the ratio $|\epsilon_2|/|\epsilon_1|$ of a double-ridge metasurface (inset), $2W = 0.45\Lambda$, $t = 0.31\Lambda$, with ω_0 ranging from $2\pi c/1.08\Lambda$ (lowest *g*) to $2\pi c/1.02\Lambda$ (highest *g*). c) The transmittance spectra were obtained using RCWA assuming absorption losses ($\epsilon_r = 2.66 - i0.026$, solid lines) and the ideal lossless case ($\epsilon_r = 2.66$, dashed lines) for GMRs (black lines) and AGMRs (red lines) around 28 GHz for TE polarization.

the AGMR can achieve a total Q-factor of up to 260. This gain can be even higher if higher index materials with lower extinction coefficient κ are used. For example, the Q_t enhancement in a double-ridge metasurface made of amorphous silicon sandwiched between water and silicon dioxide, which is a successful configuration for biosensing applications,[6] is as high as 12× (see Section S5, Supporting Information).

3. Experimental Results

To experimentally demonstrate the benefits of Fourier control of air modes, three dielectric metasurfaces were fabricated and characterized in the microwave regime, as illustrated in **Figure 6**a–c, where (a) shows the highest measurable GMR Q_t single-ridge metasurface, (b) the AGMR intermediate-Q_t double-ridge

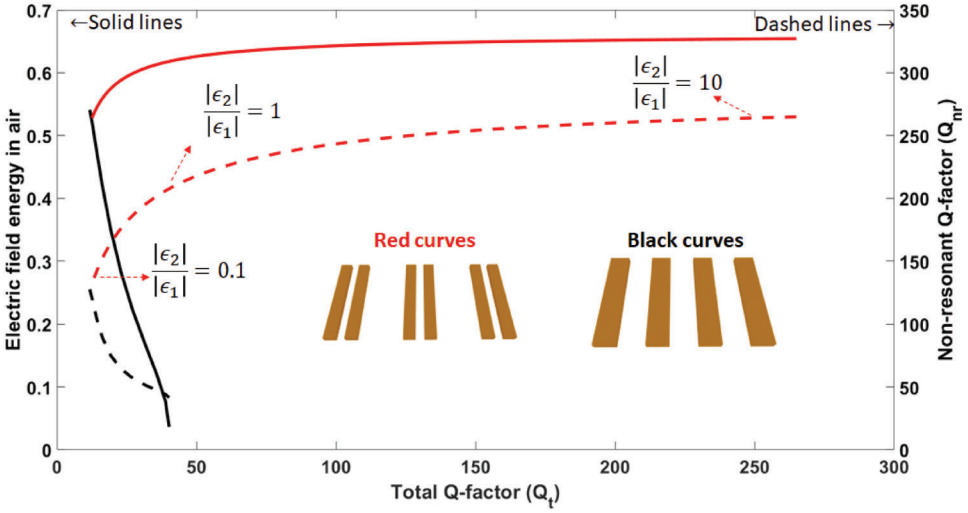

Figure 5. Energy confinement (solid lines) in air and nonresonant Q-factor (Q_{nr}, dashed lines) as function of the total Q-factor (Q_t). Black curves represent the GMR supported by the single-ridge metasurface, while red curves represent the AGMR supported by the double-ridge metasurface of Figure 4a,b, respectively. The red arrows show the Fourier components ratio for the highlighted points. TE polarization was assumed.

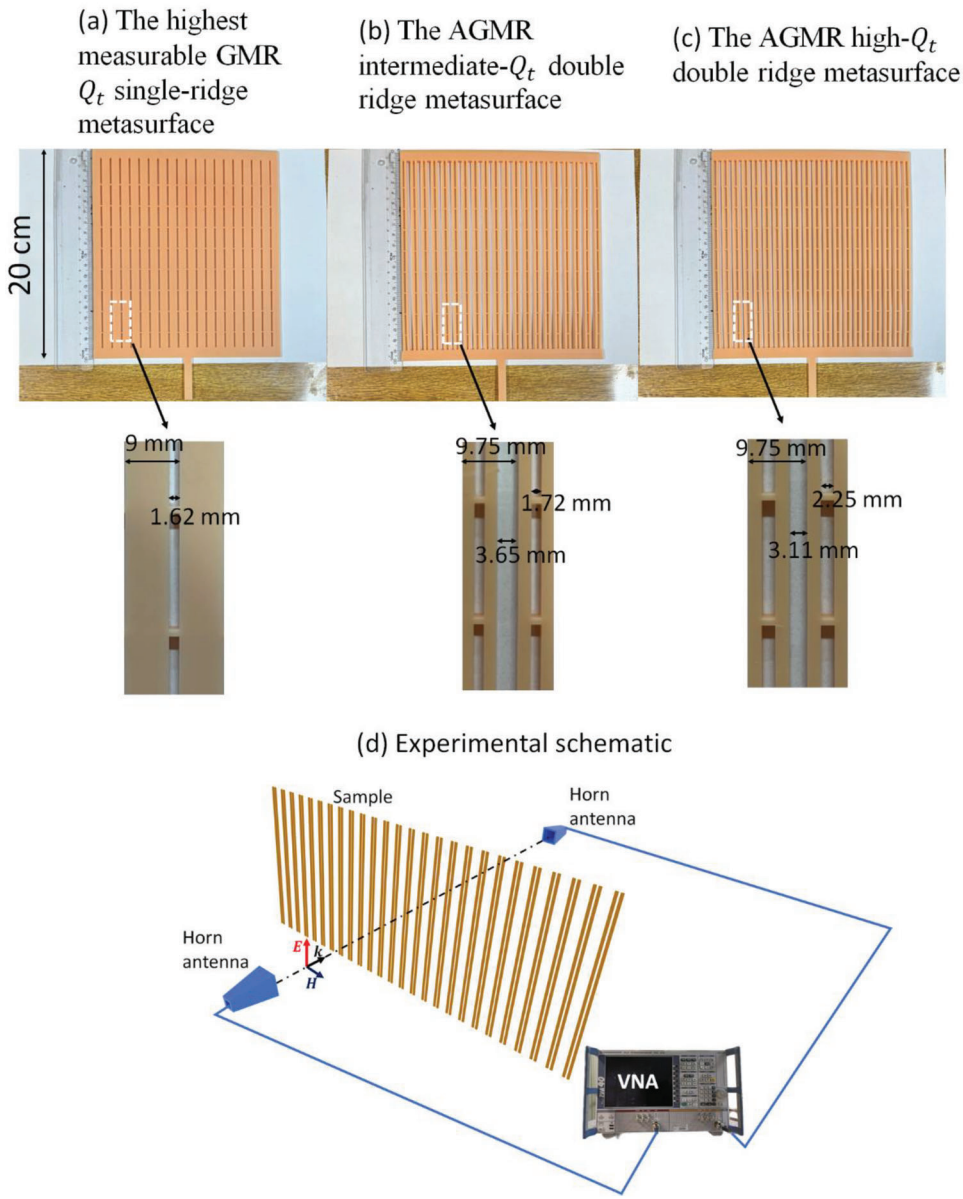

Figure 6. Fabricated samples of the a) single-ridge metasurface supporting the highest measurable GMR Q_t, b) double-ridge metasurface supporting an AGMR with intermediate Q_t (same Q_r as the GMR), and c) double-ridge metasurface supporting an AGMR with high Q_t (same resonance amplitude as the GMR). All samples were fabricated using ridges 3 mm thick. The insets show the values of the periods and gap widths of each structure. d) Schematic of the extinction spectra measurements setup to obtain the resonances, where the antenna connected to the output port of the VNA converts the transmission line signal into a free-space electromagnetic wave. The orientation of the electric field ***E*** (parallel to the dielectric ridges), magnetic field ***H*** (parallel to the direction of periodicity), and wavevector ***k*** (orthogonal to the ***E***–***H*** plane) are also indicated.

metasurface, and (c) the AGMR high-Q_t double-ridge metasurface. They were fabricated using a photocurable 3D printing resin of electrical permittivity $\epsilon_r = 2.66 - i0.08$ (see Section S6, Supporting Information) in the 26–32 GHz band. The ridge thickness is $t = 3$ mm, the period of the single-ridge structure is 9 mm, and the period of the double-ridge structure is 9.75 mm, which allows us to access modes in the desired frequency band. The gap widths of each structure can be found in the insets of Figure 6a–c. Small support sections had to be included in the small air gaps of the structures to prevent the gaps from collapsing during the sample fabrication. Such support sections, however, do not alter the metasurface's resonance parameters significantly (see Section S7, Supporting Information). To obtain the resonances, extinction spectra measurements ($1 - |S_{21}|^2$, where S_{21} is the zero-order transmission amplitude) were conducted using a Rode & Schwarz ZVA 40 Vector Network Analyzer (VNA) and two gain horn antennas to generate and receive a plane wave in free space, as illustrated in Figure 6d. More details on the fabrication and measurement methods can be found in the Experimental Section.

Table 1. Mode parameters of the metasurface supporting the highest measurable GMR Q_t, AGMR intermediate-Q_t and high-Q_t double-ridge metasurfaces of Figure 6 obtained using simulations. TE polarization was assumed.

	Highest measurable GMR Q_t	AGMR intermediate Q_t (double ridge)	AGMR high Q_t (double ridge)
Resonant Q-factor (Q_r)	107	107	575
Non-resonant Q-factor (Q_{nr})	50	233	258
Total Q-factor (Q_t)	33	73	177
Amplitude (A)	0.48	0.79	0.47
Electric energy confined in air (%)	14.76	63.67	65.07

The single-ridge metasurface was optimized to access its highest measurable GMR Q_t ($Q_t = 33$), i.e., the highest Q_t with a measurable resonance amplitude. This was achieved with a design Q-factor $Q_r = 107$, which is also the Q_r of the AGMR intermediate-Q_t double-ridge metasurface. Thus, by comparing two resonances with the same Q_r, we can assess the benefit of lower losses (higher Q_{nr}) associated with the AGMR. Furthermore, we also design a double-ridge metasurface supporting an AGMR with a higher Q_r so as to obtain the same resonance amplitude of the GMR. Thus, by comparing two resonances with the same amplitude, we can better assess the benefit of lower losses in terms of accessible Q_t.[16] The simulated values of Q_t, Q_{nr}, Q_r, the resonance amplitude A and the ratio of the electric field confined in the air gaps of all three metasurfaces are listed in **Table 1**.

The measured spectra of the metasurfaces are shown as solid black lines in **Figure 7**, which also shows the simulated resonances with (dashed blue line) and without (dashed red lines) material losses. Comparing Figure 7a,b we note that, even though

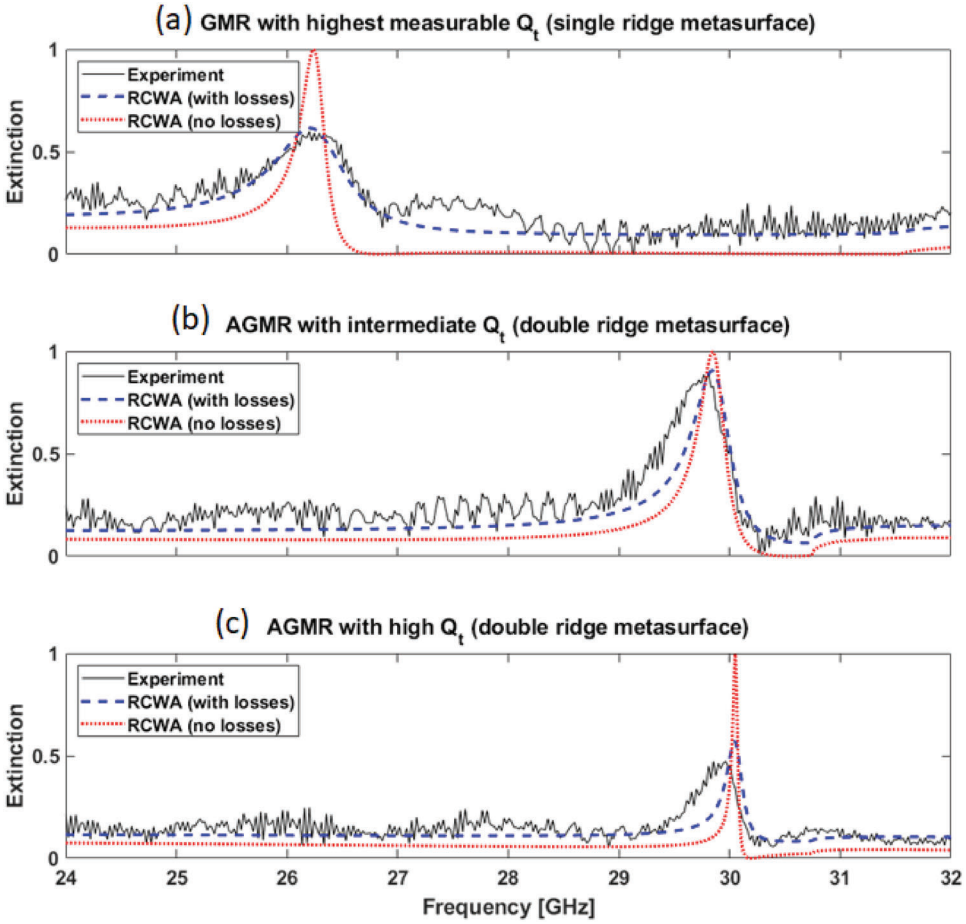

Figure 7. Measured (black solid lines) and simulated extinction spectra with (blue dashed lines) and without (red dotted lines) material losses for a) single-ridge metasurface supporting the GMR with highest measurable Q_t, b) double-ridge metasurface supporting AGMRs with intermediate Q_t (same Q_r as the GMR), and c) high Q_t (same resonance amplitude as the double ridge defined in Figure 6).

the GMR and AGMR have the same Q_r, the higher modal losses of the GMR (Figure 7a) leads to a weaker resonance amplitude and a modest Q_t (the measured resonance amplitude is $A = 0.38$ and measured $Q_t = 29$, see Table 1 for theoretical values), whereas the lower modal losses of the AGMR (Figure 7b) leads to significantly higher amplitudes and Q_t (measured values are $A = 0.73$ and $Q_t = 61$, see Table 1 for theoretical values; for more details on the methods used to obtain A and Q_t, see Section S8, Supporting Information). Furthermore, the AGMR Q_t supported by the double-ridge metasurface can be pushed to as high as 97 (Figure 7c, the difference between experiment and theory is due to the finiteness of the sample, see Section S9, Supporting Information) until the amplitude $A = 0.36$ becomes comparable to the amplitude of the GMR, which corresponds to an experimentally demonstrated Q_t enhancement of 3.3× of the AGMR over the GMR.

We notice that our material loss tangent is much higher than the state of the art in the microwave regime (e.g., our loss tangents are 30× higher than in refs.[13,15] and 20× higher than in ref.[14]). Nevertheless, even with such higher losses, our resonances are still comparable to the state of the art,[13–15] thus showing that Fourier control of air modes is a viable, simple, and versatile strategy to achieve high-Q resonances in lossy metasurfaces.

4. Conclusions

We have introduced the concept of AGMR with Fourier control of Q-factor by exploring the excitation of AGMR in double-ridge metasurfaces. The energy of these modes is confined mostly in the air gap between the ridges and, as such, leads to a minimization of the wave interaction with the structure material (lossy resin) allowing the designer to tune the Q-factor with no concomitant increase in modal losses. The proposed method results in Q_t enhancements up to 12× in amorphous silicon metasurfaces and up to 5.4× in 3D printing resin metasurfaces. Furthermore, we have experimentally demonstrated a 3.3× enhancement of Q_t in a 3D resin metasurface without sacrificing the resonance amplitude. Our analysis show that metasurfaces supporting AGMR opens the possibility of using lossy materials to obtain high-Q metasurfaces, thus widening the range of materials available for metasurface design and applications. These results, combined with the intrinsically higher sensitivity of air modes, make AGMRs a promising route for further advances in metasurface research and applications.

5. Experimental Section

The radiative Q-factor Q_r was obtained using the commercial software COMSOL Multiphysics "Eigenfrequency" study and the "Electromagnetic Waves, Frequency Domains" physics toolbox, while the simulations of the extinction spectra were obtained using an in-house implemented version of the Rigorous Coupled Wave Analysis (RCWA) method,[47,50] The samples were fabricated using a commercial Anycubic Photon Mono 6k 3D printing machine and the Anycubic Craftsman Resin. The material complex permittivity was obtained using a nonresonant permittivity retrieval method,[51] see Section S6 (Supporting Information). After printed, the structures were washed in 99.8% isopropyl alcohol and cured in UV light for 2 min each. The samples were limited to the repetition of 20 periods due to the finite printing volume of the machine.

The extinction measurements were made using a Rode & Schwarz ZVA 40 VNA to generate, receive, and process microwave signals. The VNA input (port 1) and output (port 2) channels were connected to two different Pasternack PE9851/2F-20 gain horn antennas, as illustrated in Figure 4d. The antenna connected to port 2 converts the signal generated by the VNA into a free-space propagating electromagnetic wave. The electric field orientation of the antenna is well defined, and the antenna is placed so that the exit electric field is parallel to the ridges. The sample was placed on top of a M-UTR120 rotation stage located between the two antennas. The distance between the antennas is 152 cm, which ensures that the distance between antenna and sample (76 cm) is larger than the antenna's Fraunhofer distance (42.6 cm). To measure the extinction spectrum of each sample, first the VNA was calibrated using the Rode & Schwarz ZV-Z54 calibration unit. Then, the antennas were aligned to match the center of the sample. The reference extinction spectrum ($R(\omega)$) which is obtained using the VNA with no sample between the antennas was first measured. Next, this procedure was repeated with the sample present to obtain the sample extinction spectrum ($S(\omega)$). Finally, the normalized extinction ($1 - |S_{21}|^2 = E(\omega)$) was calculated by dividing the sample extinction by the reference extinction

$$E(\omega) = \frac{S(\omega)}{R(\omega)} \tag{9}$$

Supporting Information

Supporting Information is available from the Wiley Online Library or from the author.

Acknowledgements

This project was supported by the São Paulo Research Foundation – FAPESP (Grant Nos. 2020/15940-2, 2020/00619-4, 2021/06121-0, and 2013/07276-1), the Brazilian National Council for Scientific and Technological Development – CNPq (307602/2021-4 and 304208/2021-3), and Coordination of Superior Level Staff Improvement – CAPES (Finance Code 001).

Conflict of Interest

The authors declare no conflict of interest.

Data Availability Statement

The data that support the findings of this study are available from the corresponding author upon reasonable request.

Keywords

absorption losses, air gap modes, Fourier properties, guided mode resonances, high-Q resonances

Received: June 30, 2023
Revised: August 22, 2023
Published online:

[1] M. R. Foreman, J. D. Swaim, F. Vollmer, *Adv. Opt. Photonics* **2015**, *7*, 168.
[2] A. Kodigala, T. Lepetit, Q. Gu, B. Bahari, Y. Fainman, B. Kanté, *Nature* **2017**, *541*, 196.
[3] A. S. Shorokhov, E. V. Melik-Gaykazyan, D. A. Smirnova, B. Hopkins, K. E. Chong, D.-Y. Choi, M. R. Shcherbakov, A. E. Miroshnichenko, D. N. Neshev, A. A. Fedyanin, Y. S. Kivshar, *Nano Lett.* **2016**, *16*, 4857.

[4] B.-B. Li, W. R. Clements, X.-C. Yu, K. Shi, Q. Gong, Y.-F. Xiao, *Proc. Natl. Acad. Sci. USA* **2014**, *111*, 14657.
[5] S. Tibuleac, R. Magnusson, *JOSA A* **1997**, *14*, 1617.
[6] D. Conteduca, I. Barth, G. Pitruzzello, C. P. Reardon, E. R. Martins, T. F. Krauss, *Nat. Commun.* **2021**, *12*, 3293.
[7] F. Yesilkoy, E. R. Arvelo, Y. Jahani, M. Liu, A. Tittl, V. Cevher, Y. Kivshar, H. Altug, *Nat. Photonics* **2019**, *13*, 390.
[8] K. Koshelev, Y. Kivshar, *ACS Photonics* **2020**, *8*, 102.
[9] D. Conteduca, S. D. Quinn, T. F. Krauss, *J. Opt.* **2021**, *23*, 114002.
[10] K. Bi, Q. Wang, J. Xu, L. Chen, C. Lan, M. Lei, *Adv. Opt. Mater.* **2021**, *9*, 2001474.
[11] J. Jin, X. Yin, L. Ni, M. Soljacic, B. Zhen, C. Peng, *Nature* **2019**, *574*, 501.
[12] Z. Liu, Y. Xu, Y. Lin, J. Xiang, T. Feng, Q. Cao, J. Li, S. Lan, J. Liu, *Phys. Rev. Lett.* **2019**, *123*, 253901.
[13] D. R. Abujetas, Á. Barreda, F. Moreno, A. Litman, J.-M. Geffrin, J. A. Sánchez-Gil, *Laser Photonics Rev.* **2021**, *15*, 2000263.
[14] M. V. Gorkunov, A. A. Antonov, V. R. Tuz, A. S. Kupriianov, Y. S. Kivshar, *Adv. Opt. Mater.* **2021**, *9*, 2100797.
[15] A. Sayanskiy, A. S. Kupriianov, S. Xu, P. Kapitanova, V. Dmitriev, V. V. Khardikov, V. R. Tuz, *Phys. Rev. B* **2019**, *99*, 085306.
[16] D. Conteduca, G. S. Arruda, I. Barth, Y. Wang, T. F. Krauss, E. R. Martins, *ACS Photonics* **2022**, *9*, 1757.
[17] A. Forouzmand, H. Mosallaei, *ACS Photonics* **2019**, *6*, 2860.
[18] E. Mikheeva, C. Kyrou, F. Bentata, S. Khadir, S. Cueff, P. Genevet, *ACS Photonics* **2022**, *9*, 1458.
[19] P. C. Wu, R. A. Pala, G. K. Shirmanesh, W.-H. Cheng, R. Sokhoyan, M. Grajower, M. Z. Alam, D. Lee, H. A. Atwater, *Nat. Commun.* **2019**, *10*, 3654.
[20] A. Martins, J. Li, A. F. Da Mota, V. M. Pepino, Y. Wang, L. G. Neto, F. L. Teixeira, E. R. Martins, B.-H. V. Borges, *Opt. Express* **2018**, *26*, 30740.
[21] H. Liang, Q. Lin, X. Xie, Q. Sun, Y. Wang, L. Zhou, L. Liu, X. Yu, J. Zhou, T. F. Krauss, J. Li, *Nano Lett.* **2018**, *18*, 4460.
[22] J. Yang, J. A. Fan, *Opt. Express* **2017**, *25*, 23899.
[23] D. Sell, J. Yang, S. Doshay, K. Zhang, J. A. Fan, *ACS Photonics* **2016**, *3*, 1919.
[24] R. Kolkowski, A. Shevchenko, *Nanophotonics* **2023**, *12*, 3443.
[25] V. R. Almeida, Q. Xu, C. A. Barrios, M. Lipson, *Opt. Lett.* **2004**, *29*, 1209.
[26] Q. Sun, H. Liang, J. Zhang, W. Feng, E. R. Martins, T. F. Krauss, J. Li, *Adv. Opt. Mater.* **2021**, *9*, 2002209.
[27] M. Scullion, T. Krauss, A. Di Falco, *Sensors* **2013**, *13*, 3675.
[28] K. Watanabe, M. Iwanaga, *Nanophotonics* **2023**, *12*, 99.
[29] J. Zhang, W. Liu, Z. Zhu, X. Yuan, S. Qin, *Opt. Express* **2014**, *22*, 30889.
[30] G. Sun, L. Yuan, Y. Zhang, X. Zhang, Y. Zhu, *Sci. Rep.* **2017**, *7*, 8128.
[31] L. Cong, R. Singh, *Adv. Opt. Mater.* **2019**, *7*, 1900383.
[32] X. Chen, W. Fan, *Nanomaterials* **2020**, *10*, 623.
[33] Y. Yang, I. I. Kravchenko, D. P. Briggs, J. Valentine, *Nat. Commun.* **2014**, *5*, 5753.
[34] T. Zheng, H. Kwon, A. Faraon, *Nano Lett.* **2023**, *23*, 5588.
[35] T. W. Ebbesen, H. J. Lezec, H. F. Ghaemi, T. Thio, P. A. Wolff, *Nature* **1998**, *391*, 667.
[36] Y. Guo, H. Liang, X. Hou, X. Lv, L. Li, J. Li, K. Bi, M. Lei, J. Zhou, *Appl. Phys. Lett.* **2016**, *108*, 051906.
[37] Y. Guo, S. Liu, K. Bi, M. Lei, J. Zhou, *Photonics Res.* **2018**, *6*, 1102.
[38] J.-C. Yan, Z.-K. Li, Y. Zhang, Y.-L. Wang, C.-P. Huang, *J. Appl. Phys.* **2019**, *126*, 213102.
[39] J.-C. Yan, Y. Zhang, X.-G. Yin, C.-P. Huang, *Phys. Rev. Appl.* **2020**, *14*, 054003.
[40] E. R. Martins, Y. Wang, A. L. Kanibolotsky, P. J. Skabara, G. A. Turnbull, I. D. W. Samuel, *Adv. Opt. Mater.* **2013**, *1*, 563.
[41] H. S. Bark, G. J. Kim, T.-I. Jeon, *Sci. Rep.* **2018**, *8*, 13570.
[42] W.-K. Kuo, C.-J. Hsu, *Opt. Express* **2017**, *25*, 29642.
[43] J. D. Joannopoulos, S. G. Johnson, J. N. Winn, R. D. Meade, *Molding the Flow of Light*, Princeton University Press, Princeton, NJ **2008**, Ch. 7.
[44] G. S. Arruda, D. Conteduca, I. Barth, Y. Wang, T. F. Krauss, E. R. Martins, *Opt. Lett.* **2022**, *47*, 6133.
[45] S.-G. Lee, R. Magnusson, *Phys. Rev. B* **2019**, *99*, 045304.
[46] M. G. Moharam, T. K. Gaylord, E. B. Grann, D. A. Pommet, *JOSA A* **1995**, *12*, 1068.
[47] D. M. Whittaker, I. S. Culshaw, *Phys. Rev. B* **1999**, *60*, 2610.
[48] R. Kazarinov, C. Henry, *IEEE J. Quantum Electron.* **1985**, *21*, 144.
[49] J. M. Luque-González, A. Sánchez-Postigo, A. Hadij-Elhouati, A. Ortega-Moñux, J. G. Wangüemert-Pérez, J. H. Schmid, P. Cheben, I. Molina-Fernández, R. Halir, *Nanophotonics* **2021**, *10*, 2765.
[50] G. S. Arruda, J. Li, A. Martins, K. Li, T. F. Krauss, E. R. Martins, *IEEE J. Photovoltaics* **2019**, *10*, 41.
[51] U. C. Hasar, *IEEE Microwave Wireless Compon. Lett.* **2017**, *27*, 201.